Optical and Quantum Electronics (2024) 56:326
https://doi.org/10.1007/s11082-023-05942-y

Enhanced sensing performance of carboxymethyl cellulose sodium to hydrogen sulphide gas and methylene blue dye by constructing CuO@ZnO core/shell heterostructure: A DFT/TD-DFT study

Rania Badry[1] · Nadra Nada[1] · Mahmoud M. El-Nahass[2] · Hanan Elhaes[1] · Medhat A. Ibrahim[3,4]

Received: 13 October 2023 / Accepted: 24 November 2023 / Published online: 29 December 2023

Abstract

Anthropogenic air and water pollution are two of the world's most serious public health threats, causing around 9 million fatalities each year. Accordingly, CuO, ZnO, and CuO@ZnO core/shell structures were optimized utilizing the time-dependent density functional theory (TD-DFT) method to study the effect of CuO@ZnO core/shell on the sensitivity of carboxymethyl cellulose sodium (CMC). Absorption spectra and optical band gap (E_g) have been investigated utilizing the TD-DFT method. The calculated E_g values for CuO and ZnO equal 1.23 and 3.29 eV, respectively, which agree well with those reported in the literature. The effects of H_2S gas and methylene blue dye (MB) adsorption on the electronic characteristics of dimer CMC /CuO@ZnO structures were investigated in terms of TDM, HOMO/LUMO energy, and molecular electrostatic potential (MESP). The TDM in dimer CMC/CuO@ZnO structure was increased to 72.152 and 67.606 Debye, while ΔE was reduced by 6.42% and 82.57% due to the adsorption of H_2S and MB dye, respectively. This means that it has a faster response to MB than to H_2S. Additionally, MESP confirms the increased reactivity of dimer CMC/CuO@ZnO due to the adsorption process. As a result, dimer CMC/CuO@ZnO structures appear to be attractive candidates for H_2S and MB dye sensing applications.

Keywords Air and water pollution · CuO@ZnO core/shell · TD-DFT · Carboxymethyl cellulose sodium · H_2S gas and MB dye

✉ Medhat A. Ibrahim
medahmed6@yahoo.com

[1] Physics Department, Faculty of Women for Arts, Science and Education, Ain Shams University, Cairo 11757, Egypt

[2] Physics Department, Faculty of Education, Ain Shams University, Roxy, Cairo, Egypt

[3] Spectroscopy Department, National Research Centre, 33 El-Bohouth St., Dokki, Giza 12622, Egypt

[4] Molecular Modeling and Spectroscopy Laboratory, Centre of Excellence for Advanced Science, National Research Centre, 33 El-Bohouth St., Dokki, Giza 12622, Egypt

1 Introduction

As a result of rapid industrialization, which has resulted in a growth in the quantity of harmful and dangerous gases in the atmosphere (Manisalidis et al. 2020; Chauhan et al. 2021; Cui et al. 2020), environmental pollution has lately reached an alarming level. Most gases are inhaled by individuals without their knowledge due to their odorless and colorless characteristics, causing major health concerns and even death (Chen et al. 2019). As a result, creating sensors and systems capable of detecting hazardous and dangerous pollutants is crucial (Badry et al. 2021). The literature has reported metal oxide semiconductor (MOS) sensors, electrochemical gas sensors, solid electrolyte gas sensors, catalytic combustion gas sensors, and others (Wan et al. 2021; Rui-Jie et al. 2021; Tamura and Imanaka 2022; Badry et al. 2022a). Since they can be used to detect a variety of gases at lower concentrations, MOS gas sensors are among the most explored of the numerous types of gas sensors (Isaac et al. 2022; Dadkhah and Tulliani 2022; Gai et al. 2022; Alsheheri et al. 2023). Because of the huge number of surface sites, most target gas molecules are adsorbed by oxygen ions that have previously been adsorbed at the metal-oxide surface. Interactions between adsorbed target species and oxygen ions can alter the charge carrier concentration, affecting the material's conductivity (Wu et al. 2022; Albargi et al. 2021; ezzat et al. 2021).

Recently, MOS sensors have been created employing p-n heterojunction structures, which use nanocomposite of both types (p- and n-type) as functional materials to enhance the sensing properties (Rani et al. 2022; Yin et al. 2021). This has allowed researchers to examine the properties of both n- and p-type semiconductors. As a result, various MOS sensors based on p–n heterojunction structures such as, MoS_2/ZnO (Kumar et al. 2021), SnO_2/Co_3O_4 (Sun et al. 2021), CuO/$CuFe_2O_4$ (Wang et al. 2022a, b), NiO/ZnO (Dey et al. 2020), Ni/WO_3 (Karaduman et al. 2022), SnO_2/CuO (Zhang et al. 2021), and others, were created and described in the literature. Because p-n heterojunction increases the electron depletion layer on the nanoparticles surface and the carrier's separation increases the active sites on the material's surface, CuO/ZnO nanoparticles demonstrated good selectivity towards H_2S gases among heterojunction nanomaterial-based MOS sensors (Navale et al. 2021; Li et al. 2018). There have been a number of documented practical studies on this p-n heterojunction for H_2S gas sensing (Li et al. 2022a, b), but to the best of our knowledge, no theoretical work on this material has been documented.

Due to their broad bandgap, piezoelectricity, high exciton binding energy, high conductivity and electron mobility, strong chemical stability, thermally stable, and biocompatibility, zinc oxide nanoparticles (ZnO) are one of the most significant and functional materials (Wang et al. 2020a, b, 2022a, b; Sharma et al. 2020; Badry et al. 2022a; Omar et al. 2022). Therefore, a variety of methods, including doping, surface modification, and the creation of composites, have been used to enhance the sensing performance of gas sensors based on ZnO (Wang et al. 2020a, b; Nemufulwi et al. 2023; Sun et al. 2023). In fact, UV radiation accounts for only 5% of the solar spectrum. As a result, it is usually desirable to improve ZnO in an attempt to make it active in the visible region. Coupling ZnO with semiconductors with a narrow band gap is one technique to boost its photoactivity under sunlight. The linked material (such as CuO) should be visible light-active and limit charge recombination (Wang et al. 2020a, b). According to the theoretical DFT study by Badry et al. (2022b), carboxymethyl cellulose sodium (CMC)-decorated ZnO is a good adsorbent for H_2S due to its higher binding energy. CMC is a water-soluble, linear cellulose ether that attracts both negative and positive charges (Amu-Darko et al. 2023) thus facilitating the adsorption of H_2S gas on its surface.

Among the most widely investigated poisonous gases are ammonia (NH_3), carbon monoxide, carbon dioxide, sulfur dioxide, and hydrogen sulfide (H_2S), which are produced by numerous sources, such as industry. H_2S gas is a highly toxic, poisonous, colorless, and deadly gas that poses a serious health risk to humans and contaminates the environment (Hosseini-Shokouh et al. 2023; Wang et al. 2023; Li et al. 2023). Inhaling H_2S gas can result in major health problems in people, including respiratory tract infections, eye irritation, asthma, heart damage, and cancer (Li et al. 2022a, b). As a result, an effective method for identifying such dangerous gases is required.

NH_3 is a natural gas that is present in the atmosphere at ppb or sub-ppb concentrations. Human activity has recently emitted the majority of the NH_3. Combustion from chemical plants and motor vehicles is one of the major sources of NH_3 emissions. Food technology, chemical plants, medical diagnosis, and environmental protection all use NH_3 sensors. NH_3 can be detected by a variety of methods. Penetrating scents may easily detect high amounts. Lower NH_3 concentrations need the use of gas sensors.

Additionally, one of the major health concerns in recent years has been the lack of access to clean drinking water. One of the most common compounds that render water unsafe for drinking is industrial dyes. Methylene blue (MB), one of these dyes, poses the greatest risk to humans and environmental security since it is poisonous, carcinogenic, and non-biodegradable (Chahar et al. 2023; Abd-Elhamid, et al. 2020; Eltaweil et al. 2023). It is typically released into natural water sources, endangering the health of both people and other living creatures. Therefore, MB removal from wastewater requires the development of an effective, ecologically friendly technology. The complete mineralization of the dye into simple, non-toxic species has the advantage of potentially lowering the cost of processing (Khan et al. 2020; Obayomi et al. 2023).

In this study, time—dependent density functional theory (TD-DFT) calculations were carried out for the optimization of CuO, ZnO, and CuO@ZnO core shell structures to study the sensitivity of dimer CMC/ CuO@ZnO core/shell to H_2S gas and MB dye.

1.1 Calculation details

The Gaussian 09 package of programs (Frisch et al. 2010) was used to study the optimized structures as well as the electronic properties of CuO@ZnO core shell, CMC/ CuO@ZnO core shell, CMC/ CuO@ZnO core shell/ NH_3, CMC/ CuO@ZnO core shell/ H_2S, and CMC/ CuO@ZnO core shell/ MB dye using density functional theory (DFT). Becke's three-parameter B3 with the Lee, Yang, and Parr (LYP) correlation functional was used in the calculations (Becke 1993a, b; Lee et al. 1988). The exchange–correlation functional is included in this B3LYP hybrid functional, which is based on the standard form of the Vosko-Wilk-Nusair correlation potential (Foresman and Frish 1996). The Slater exchange was originally included in functional B, as were corrections affecting the density gradient. Lee, Yang, and Parr developed a correlation functional LYP that contains both local and nonlocal terms (Vosko et al. 1980). The standard LANL2DZ basis set was employed for all structures. The optical absorption spectrum, total dipole moment (TDM), and the energy difference between the highest occupied molecular orbital (HOMO) and the lowest unoccupied molecular orbital (LUMO) were used to calculate the energy gap (HOMO/LUMO), and molecular electrostatic potentials (MESPs) were calculated for CuO, ZnO and CuO@ZnO core shell before and after gas absorption. The optical absorption spectrum and optical band gap energy were calculated using Time-Dependent Density Functional Theory (TD-DFT) at the same level of theory.

2 Results and discussion

2.1 Building model molecules

Through the coupling of optical, semiconducting, and piezoelectric properties to tune charge carrier generation, recombination, and transportation at an interface, the piezo-phototronic influence has been used to enhance the performance of optoelectronic devices (Becke 1993a, b; Feng et al. 2013). Model molecules representing CuO and ZnO are shown in Fig. 1a and b. Despite its excellent piezoelectric capabilities, the UV area is the only place where ZnO and CuO can be used as a photo-detector. To get over this constraint, a core/shell system was used, such as a CuO@ZnO core/shell with enough phot-absorption in the narrow band gap of the ZnO shell layer. The construction of core/shell structures has led to such rapid advancement in the sciences that they are referred to as magical mixtures. The optimized structure of the CuO@ZnO core/shell is presented in Fig. 1c. In earlier research, the effect of ZnO on the electronic properties of CMC was simulated using two units of CMC (Badry et al. 2022b). Consequently, two units of CMC were used to replicate the CuO@ZnO core/shell effect in this study. To investigate the interaction between the CuO@ZnO core/shell and the H_2S, NH_3 and HBr gases and MB dye, a core/shell consisting of 16 atoms ($Zn_6Cu_2O_8$) was chosen.

2.2 Excited state analysis and electronic properties of CuO, ZnO and CuO@ZnO core/shell

The optical features of the CuO@ZnO core/shell were explored before the study of sensitivity to H_2S gas and MB dye. As a result, molecular excitation was investigated for CuO, ZnO, and CuO@ZnO core/shell. CuO and ZnO have sharp peaks at 675 and 324 nm, respectively as a dominant transition, which is shifted to 1262 nm for the CuO@ZnO core/shell structure calculated utilizing the B3LYP method (Fig. 2). Almost every peak indicated a sequence of transitions from ground to excited states. The large shift in the absorption peak confirms that the molecular structure of CuO was changed due to the formation of the ZnO shell layer. The optical band gap computed using the TD-DFT, of the three models is presented in Fig. 3. Table 1 shows the calculated absorption wavelength and optical bandgap energy of CuO, ZnO, and CuO@ZnO core/shell supposed models. As indicated in the table, the optical bandgap energy of CuO@ZnO core/shell (0.650 eV) is

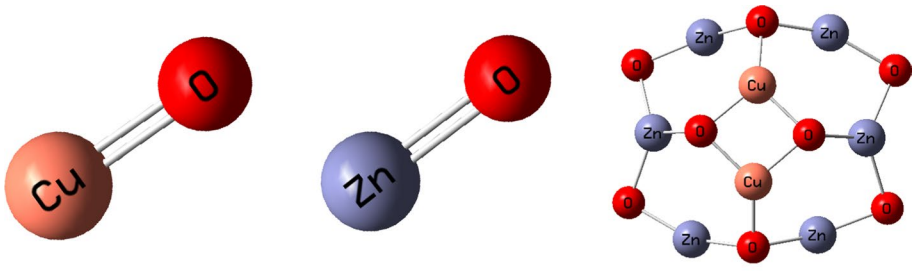

Fig. 1 The optimized structure of **a** CuO, **b** ZnO, and **c** CuO@ZnO core/shell

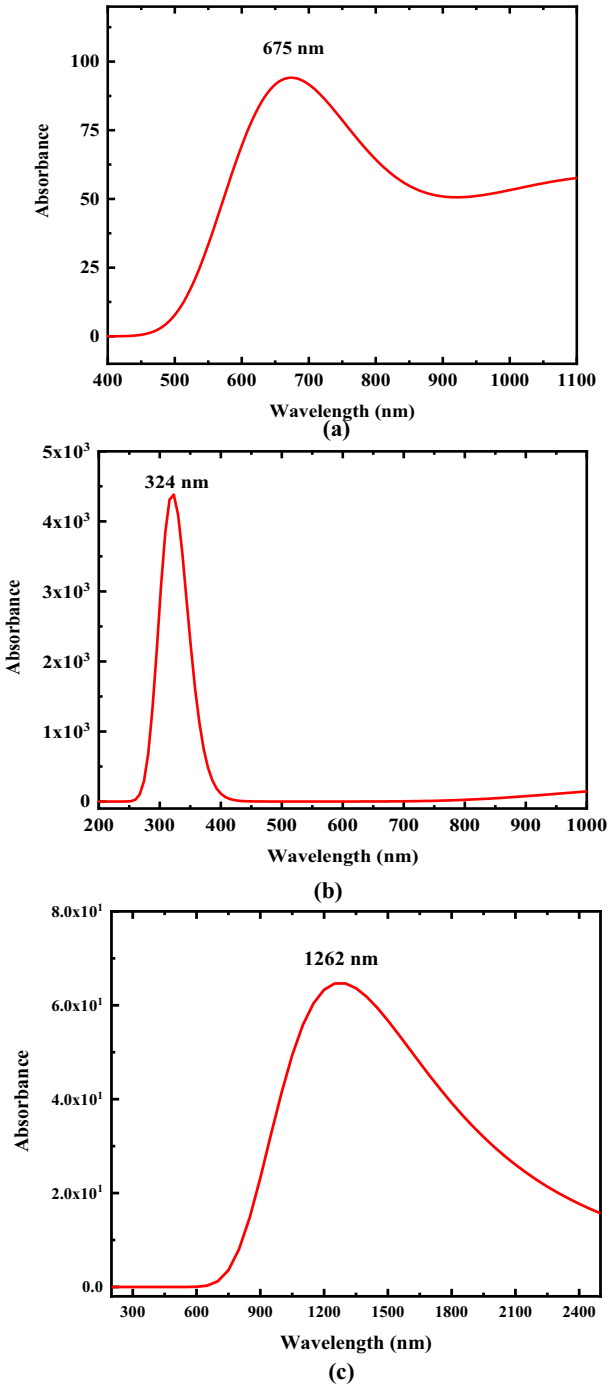

Fig. 2 B3LYP/Lanl2dz calculated UV–Vis absorbance spectra of **a** CuO; **b** ZnO and **c** CuO@ZnO core/shell

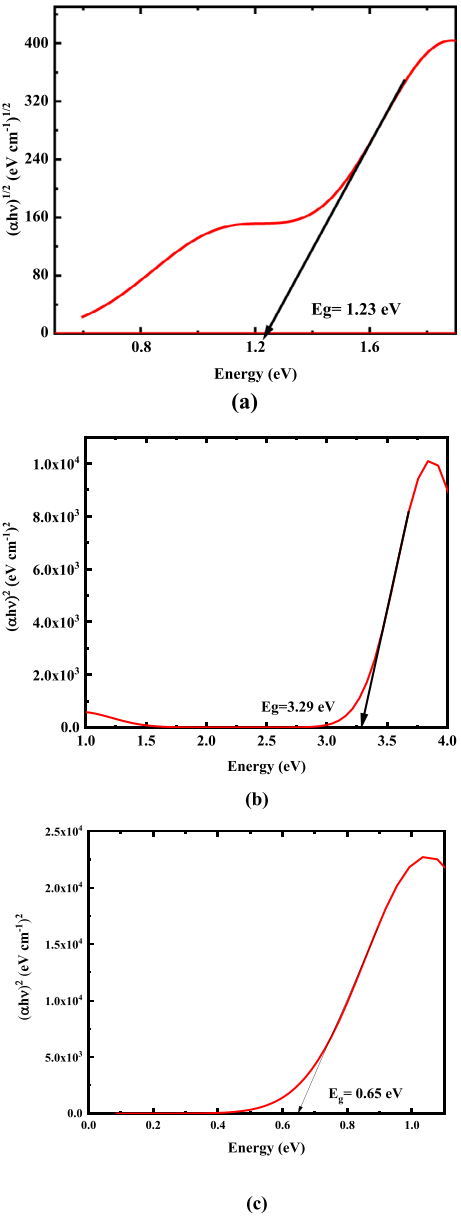

Fig. 3 B3LYP/Lanl2dz calculated optical band gaps of **a** CuO; **b** ZnO and **c** CuO@ZnO core/shell

Table 1 B3LYP/Lanl2dz calculated maximum absorption wavelength (λ_{max}) and optical bandgap energy (E_g), for CuO, ZnO and CuO@ZnO core/shell model molecules

Structure	λ (nm)	E_g (eV)
CuO	675	1.230
ZnO	324	3.290
CuO@ZnO	1262	0.650

lower than that of CuO (1.230 eV) and ZnO (3.290 eV), which is in good agreement with the experimental data due to the formation of localized states within the bandgap.

Additionally, TDM and electronic bandgap energy are calculated and presented in Table 2. All these physical parameters are considered strong indicators in studying the sensitivity and reactivity of different structures. CuO has a TDM of 5.284 Debye, while ZnO and CuO@ZnO core/shell possess a TDM of 5.831 and 0.240 Debye, respectively. It can be noticed from the table that the CuO@ZnO core/shell's HOMO/LUMO bandgap is higher than that of CuO. This is due to the formation of a shell layer with a wide bandgap on the CuO surface, which acts as an absorption layer (Badry et al. 2022b). Improving the charge carrier collection favored by radial geometry, where electrons and holes are spatially constrained in different conducting channels of hetero-structures, which results in reduced recombination losses, is made possible by the strategy of using core/shell architecture. Thus, building molecules based on polymers and core/shell structures is increasingly gaining popularity because they are at the cutting edge of materials chemistry and several other disciplines, including electronics, optics, biomedicine, and catalysis (Jung et al. 2017; Wu et al. 2011).

2.3 Electronic properties of CMC/CuO@ZnO core/shell

The construction of core/shell structures has led to such rapid advancement in the sciences that they are referred to as magical mixtures. It is reported that the CMC's electronic properties changed with changing the interaction site as a result of interaction with ZnO (Badry et al. 2022b). Accordingly, the proposed dimer CMC structure has eight active sites based on the acquired MESP maps of dimer CMC. They also confirmed that, due to the significant improvement in its electronic properties, the dimer CMC/P_2 OZn model molecule can be employed in a variety of applications (Badry et al. 2022b). Thus, interaction between CMC and the CuO@ZnO core/shell was accomplished through this OH group. However, other researchers proposed that the interaction of metal oxides can be accomplished either through the metal atom or the oxygen one (Alsheheri et al. 2023; Refaat et al. 2019). Accordingly, there are two possibilities of CMC interaction with the CuO@ZnO core/shell. The first interaction mechanism occurs via: the hydrogen atom of CMC' hydroxyl group and the oxygen atom of the shell.

The other hypothesis is that an interaction occurred between the CMC hydroxyl group's oxygen and the Zn atom of the CuO@ZnO core/shell. The two hypotheses where the CuO@ZnO core/shell molecule may connect with the CMC's hydroxyl group via its O or Zn site are depicted in Fig. 4. The calculated energy gap between the CMC/CuO@ZnO structure's highest-occupied molecular orbital and the lowest-unoccupied molecular orbital (HOMO/LUMO) was determined to be 0.212 and 0.218 eV, for the interaction proceeds through the oxygen and Zn atoms of the CuO@ZnO core/shell, respectively (see Table 3). The obtained values of the dimer CMC/CuO@ZnO model's HOMO/LUMO bandgap

Table 2 B3LYP/Lanl2dz calculated HOMO/LUMO bandgap (ΔE) as eV and total dipole moment (TDM) as Debye for CuO, ZnO and CuO@ZnO core/shell model molecules

Structure	ΔE (eV)	TDM (Debye)
CuO	1.358	5.284
ZnO	5.412	5.831
CuO@ZnO	1.466	0.240

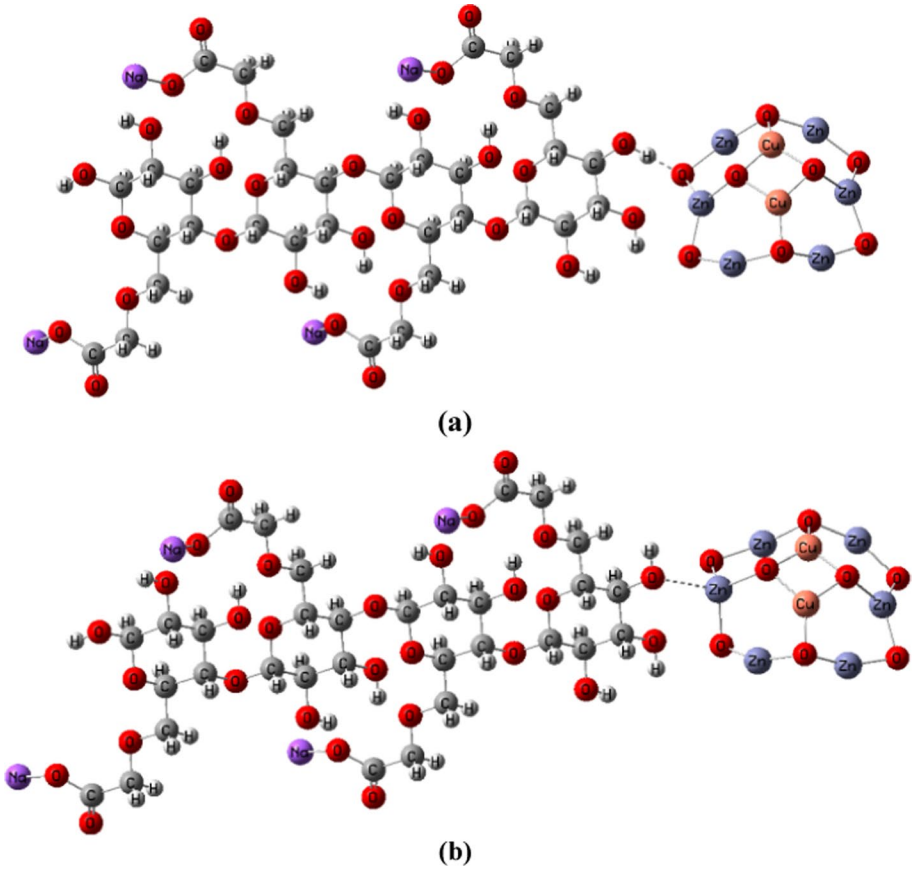

Fig. 4 Optimized structure of **a** dimer CMC- (P_{H^-O}) core/shell, and **b** dimer CMC- (P_{O-Zn}) core/shell

Table 3 B3LYP/Lanl2dz calculated total dipole moment (TDM) as Debye and HOMO/LUMO bandgap energy by as (eV) for CMC, CMC/ P_X CuO@ZnO core/shell. Where, P_x refers to the interaction location between CMC and CuO@ZnO core/shell (i.e. X = O–Zn and H–O)

Structure	ΔE (eV)	TDM (Debye)
2 CMC	0.449	9.074 (Badry et al. 2022b)
2 CMC- P_2 OZn	0.265	35.171 (Badry et al. 2022b)
dimer CMC- (P_{H-O}) core/shell	0.212	64.568
dimer CMC- (P_{O-Zn}) core/shell	0.218	67.282

energy are less than those of both the dimer CMC structure and dimer CMC interacted with ZnO only at the same interaction position.

To further explore how the CuO@ZnO core/shell affects the CMC electronic characteristics, TDM was calculated. Table 3 shows the calculated values of TDM for dimer CMC-CuO@ZnO core/shell structures for the two interaction mechanisms (i.e., dimer CMC-(P_{H-O}) CuO@ZnO and dimer CMC- (P_{O-Zn}) CuO@ZnO). It is clear that the formation of

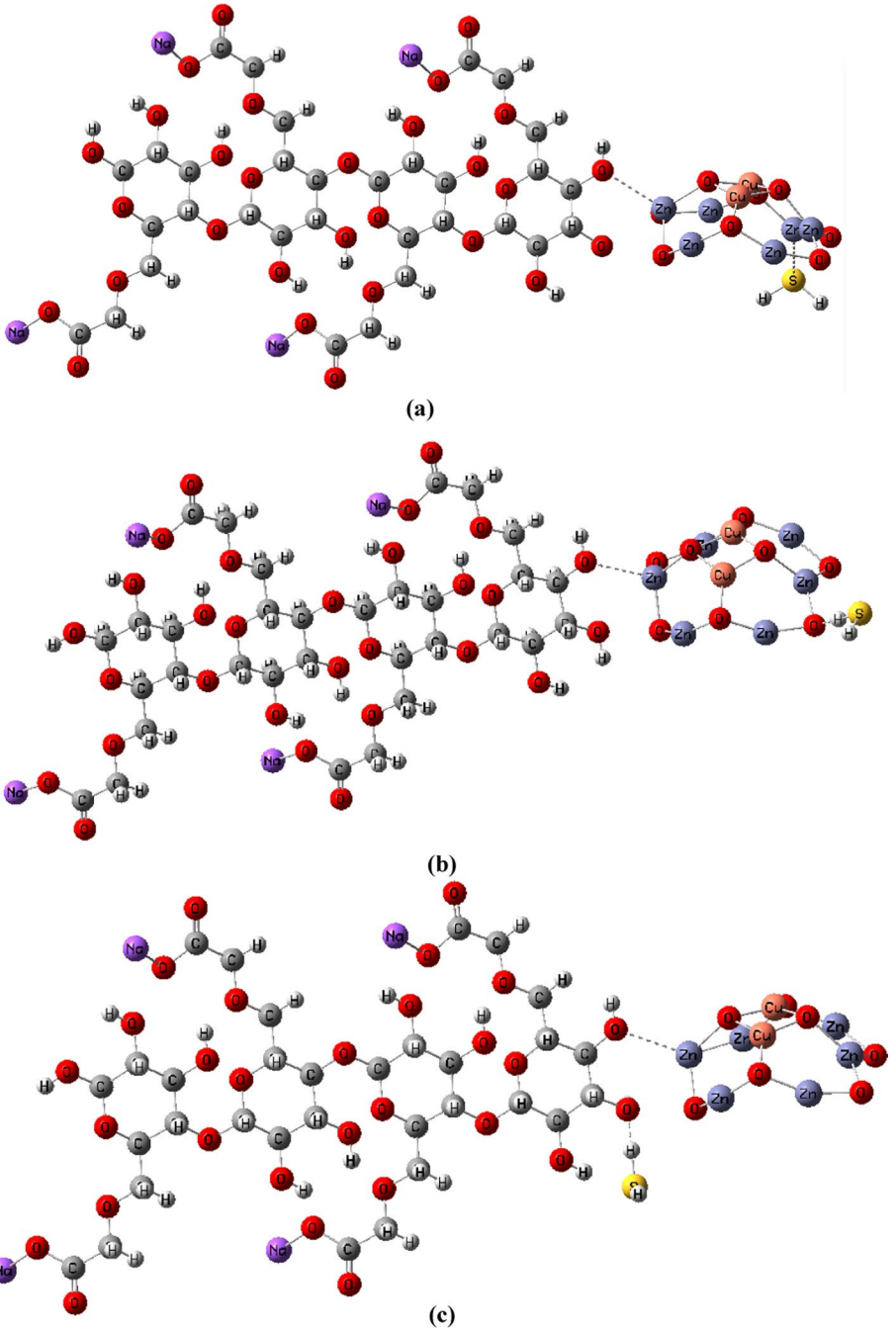

Fig. 5 Optimized structure of H_2S gas adsorption on the dimer CMC /CuO@ZnO core/shell structure' surface at different locations i.e. **a** dimer CMC- ($P_{O–Zn}$) core/shell—($P_{Zn–S}$) H_2S, **b** dimer CMC- ($P_{O–Zn}$) core/shell—($P_{Shell\ O–H}$) H_2S, **c** dimer CMC- ($P_{O–Zn}$) core/shell—($P_{OH\ Left\ side}$) H_2S, **d** dimer CMC- ($P_{O–Zn}$) core/shell—($P_{OH\ Right\ side}$) H_2S, **e** dimer CMC- ($P_{O–Zn}$) core/shell—($P_{Shell\ O–H}$) NH_3 gas, and **f** dimer CMC-($P_{O–Zn}$) core/shell—($P_{Shell\ O–H}$) HBr gas

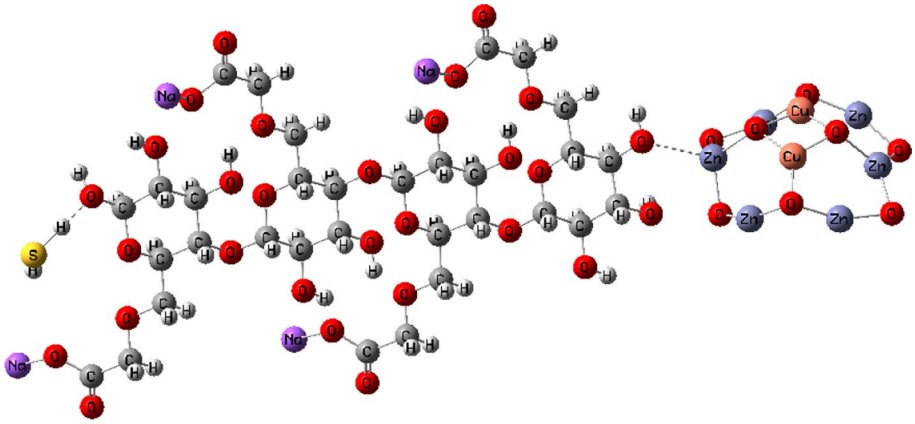

(d)

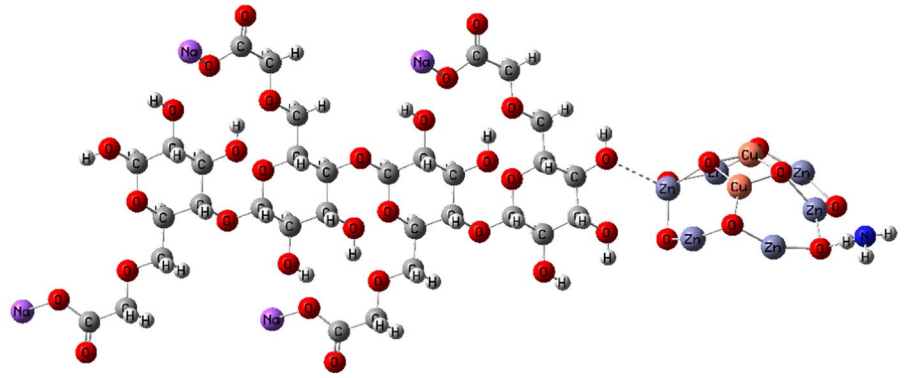

(e)

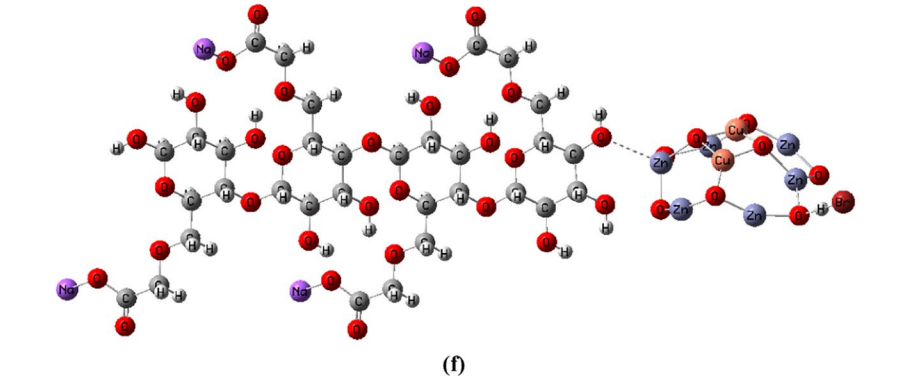

(f)

Fig. 5 (continued)

Table 4 B3LYP/Lanl2dz calculated total dipole moment (TDM) as Debye and HOMO/LUMO bandgap energy as (eV) for dimer CMC/ $P_{O–Zn}$ CuO@ZnO interacted with H_2S gas at different locations

Structure	ΔE (eV)	TDM (Debye)
H_2S gas	8.194 (Badry et al. 2022b)	1.939 (Badry et al. 2022b)
dimer CMC- ($P_{O–Zn}$) core/shell—(P_{Zn-S}) H_2S	0.211	54.444
dimer CMC- ($P_{O–Zn}$) core/shell—($P_{Shell\ O–H}$) H_2S	0.229	72.152
dimer CMC- ($P_{O–Zn}$) core/shell—($P_{OH\ Left\ side}$) H_2S	0.204	58.372
dimer CMC- ($P_{O–Zn}$) core/shell—($P_{OH\ Right\ side}$) H_2S	0.220	67.188
dimer CMC- ($P_{O–Zn}$) core/shell—(P_{OH}) NH_3	0.227	66.644
dimer CMC- ($P_{O–Zn}$) core/shell—(P_{OH}) HBr	0.231	73.607

a core/shell structure has a great effect on the CMC's physical properties. As the TDM of dimer CMC increased from 9.074 Debye to 64.568 and 67.282 Debye, for the interaction preceded through the O and Zn atoms of the CuO@ZnO core/shell, respectively. The highest values of the TDM mean the highest electronegativity. So, due to the high functionality of core/shell structures with modified properties, it can be concluded that the dimer CMC ($P_{O–Zn}$) CuO@ZnO structure is a suitable candidate for gas sensing properties as well as dye removal.

2.4 Sensitivity of CMC/CuO@ZnO core/shell to H_2S, NH_3, and HBr gases

It has been noted that the shift in the HOMO/LUMO bandgap energy throughout the adsorption process is connected to the sorbent's sensitivity to the adsorbate. As a consequence, the conductivity is considerably impacted by the decrease in the CMC/CuO@ZnO core/shell structure's ΔE and increased TDM values. There are various locations where the H_2S molecule and the dimer CMC- ($P_{O–Zn}$) CuO@ZnO core/shell structure can interact, as shown in Fig. 6. As mentioned previously, this polymer nanocomposite of CMC/CuO@ZnO is composed of two units of CMC and one CuO@ZnO core/shell molecule, which have various positions for H_2S gas absorption. Figure 5 displays these positions. Any one of these four sites may be occupied by gas and/or MB dye. Every possibility is simulated in the case of H_2S gas sensor. These interaction possibilities are those that occurred via the Zn atom of the core/shell and the S atom of the H_2S gas, the O atom of the shell and the H atom of H_2S gas, and the other OH groups at the terminals of the CMC structure (OH groups at the left and right sides of CMC), respectively.

The adsorption of the H_2S molecule in the gas phase results in a considerable change in the HOMO/LUMO bandgap of the CMC - ($P_{O–Zn}$) CuO@ZnO core/shell structure. As it's values changed to 0.211, 0.229, 0.204, and 0.220 eV, for the structures represent dimer CMC- ($P_{O–Zn}$) core/shell- H_2S gas in the different four hypotheses of interaction, i.e., dimer CMC- ($P_{O–Zn}$) core/shell—($P_{Zn–S}$) H_2S, dimer CMC- ($P_{O–Zn}$) core/shell—($P_{Shell\ O–H}$) H_2S, dimer CMC- ($P_{O–Zn}$) core/shell—($P_{OH\ Left\ side}$) H_2S and dimer CMC- ($P_{O–Zn}$) core/shell—($P_{OH\ Right\ side}$) H_2S, respectively. Thus, the charge transfer from the CuO@ZnO core/shell to the dimer CMC structure was simpler than that from the CMC/CuO@ZnO core/shell to H_2S gas, due to the narrowing of the energy gap between the HOMO and the LUMO of the dimer CMC/CuO@ZnO structure. However, the reverse situation was observed for the

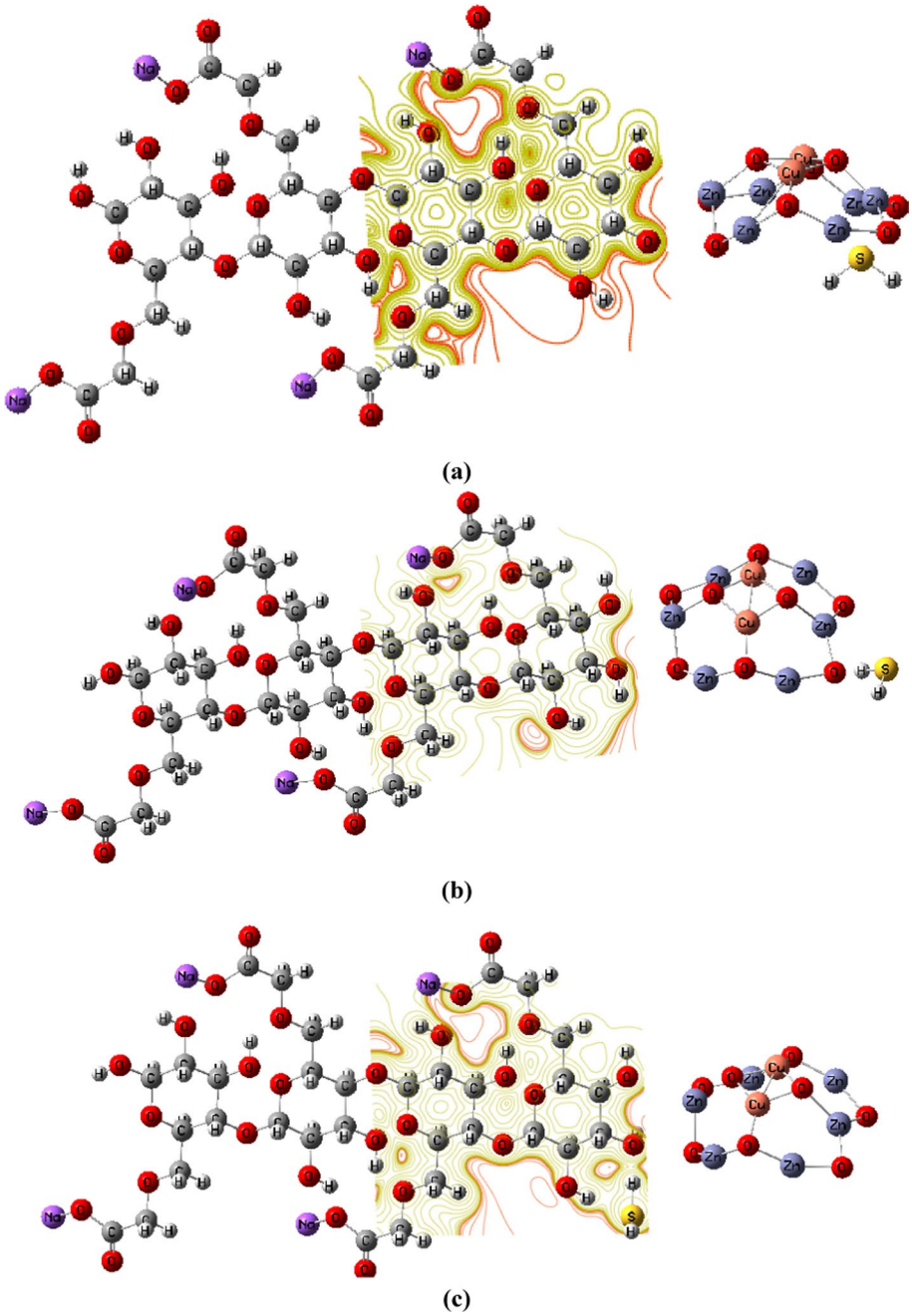

Fig. 6 MESP maps for the structure representing H_2S gas adsorption on the dimer CMC /CuO@ZnO core/shell structure's surface at different locations: **a** dimer CMC- ($P_{O–Zn}$) core/shell—($P_{Zn\text{-}S}$) H_2S, **b** dimer CMC- ($P_{O–Zn}$) core/shell—($P_{Shell\ O–H}$) H_2S, **c** dimer CMC- ($P_{O–Zn}$) core/shell—($P_{OH\ Left\ side}$) H_2S, **d** dimer CMC- ($P_{O–Zn}$) core/shell—($P_{OH\ Right\ side}$) H_2S as contour action, **e** dimer CMC- ($P_{O–Zn}$) core/shell—($P_{Shell\ O–H}$) NH_3 gas, and **f** dimer CMC- ($P_{O–Zn}$) core/shell—($P_{Shell\ O–H}$) HBr gas

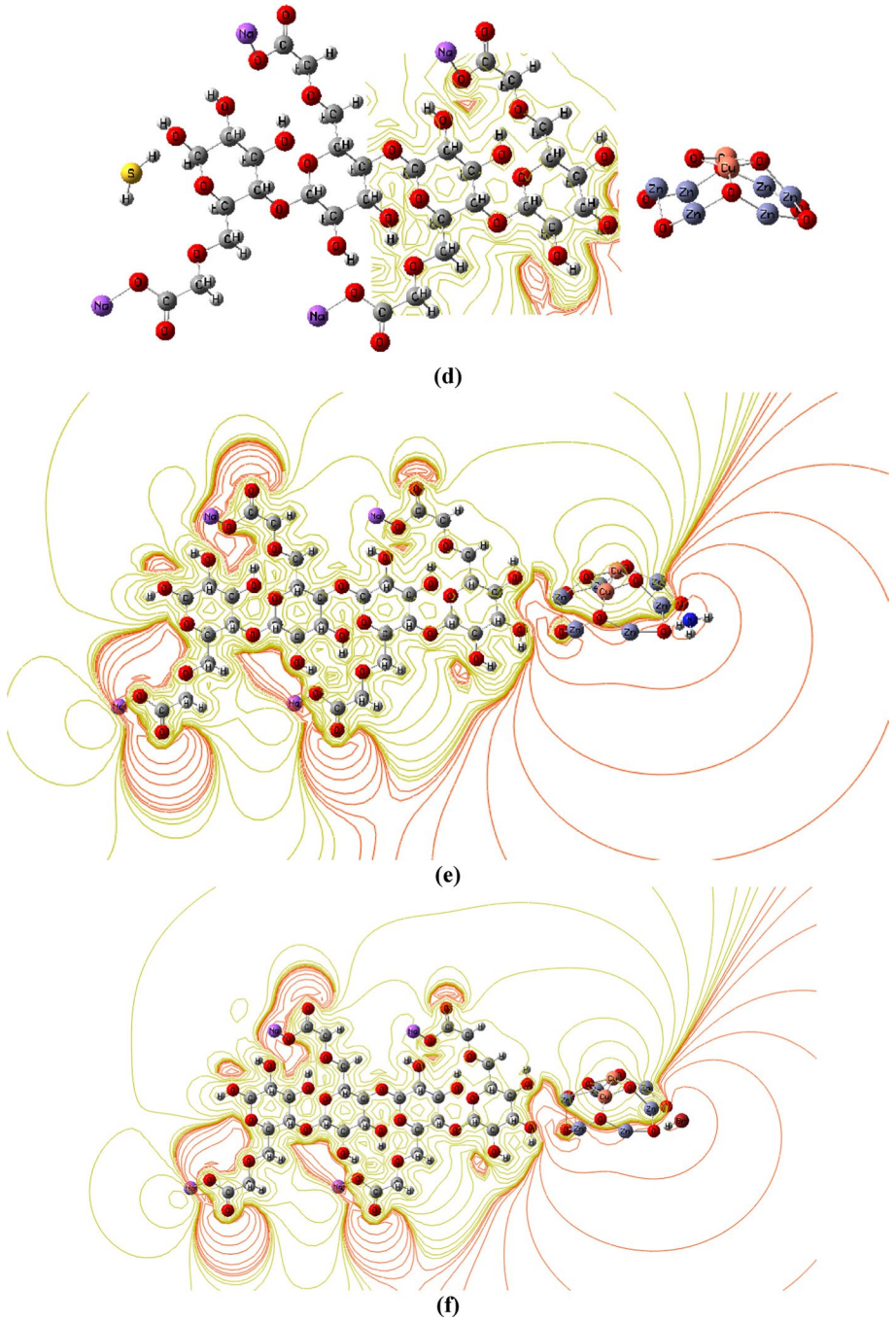

Fig. 6 (continued)

Fig. 7 Optimized structure of MB dye adsorption on the dimer CMC /CuO@ZnO core/shell structure' surface at different locations: **a** MB dye, **b** dimer CMC- ($P_{O–Zn}$) core/shell—($P_{O–N}$) MB, **c** dimer CMC- ($P_{O–Zn}$) core/shell—($P_{O–S}$) MB and **d** dimer CMC- ($P_{O–Zn}$) core/shell—(P_{OH}) MB

TDM values. Table 4 shows that the TDM values were dramatically increased as a result of the H_2S molecule adhering to the dimer CMC- ($P_{O–Zn}$) core/shell structure. The structure representing dimer CMC- ($P_{O–Zn}$) core/shell—($P_{Shell\ O-H}$) H_2S has a TDM of 72.152 Debye. This value decreased slightly when the interaction position changed to OH groups located at the left and right side terminals of the CMC's structure.

Additionally, the sensitivity of the dimer CMC/CuO@ZnO core/shell structure to another toxic gases such as NH_3 and HBr was studied at the same level of theory. Figure 5 e and f present the proposed model molecule of dimer CMC/CuO@ZnO core/shell exposed to NH_3 gas and HBr gas, respectively. When the surface of the dimer CMC/CuO@ZnO model is exposed to a single molecule of NH_3 gas, the TDM of dimer CMC/CuO@ZnO changes to 66.644 Debye, while ΔE changes to 0.227 eV (Table 4). This confirms that the dimer CMC/CuO@ZnO surface is sensitive to NH_3 gas. As a result, it has been concluded that the dimer CMC/CuO@ZnO model molecule might be employed as a gas sensor for NH_3.

In a similar context, the sensitivity of the dimer CMC/CuO@ZnO model molecule to HBr gas is investigated at the same theoretical level. Because of exposure to HBr gas, the TDM of dimer CMC/CuO@ZnO changed to 73.607 Debye, while the ΔE changed to 0.231 eV.

At the B3LYP/Lanl2dz level, molecular electrostatic potential (MESP) maps were calculated. MESP is a molecular modeling parameter that successfully tests the examined structure's compatibility and reactivity with its surroundings (gases and other pollutants) by identifying its potential active sites. More specifically, MESP maps are distinguished by their important capacities for depicting the distribution of electronic charges throughout the studied structure and indicating the most likely active locations.

Figure 6 depicts the MESP maps of H_2S gas adsorbed over the entire surface of the dimer CMC-($P_{O–Zn}$) CuO@ZnO structure using the MESP maps. These maps employed various colors to depict the various values of the MESP (red, yellow, green, light blue, and dark blue). Red and yellow colors were utilized in association with an electrophilic attack for negative values of the MESP; blue (light and dark) colors were utilized with a nucleophilic attack for positive MESP; and green color indicates neutral MESP (Politzer et al. 1985; Weiner et al. 1982; Pullman and Pullman 1981).

The MESP map demonstrates that the H_2S gas adsorbate confirms that nucleophilic reactions are the most common for the interactions that proceed through the core/shell's oxygen and the hydrogen of the gas dimer CMC- ($P_{O–Zn}$) core/shell—($P_{Shell\ O–H}$) H_2S

Table 5 B3LYP/Lanl2dz calculated total dipole moment (TDM) as Debye and HOMO/LUMO bandgap energy as (eV) for dimer CMC/ $P_{O–Zn}$ CuO@ZnO core/shell interacted with MB dye at different locations

Structure	ΔE (eV)	TDM (Debye)
MB Dye	1.822	1.646
dimer CMC- ($P_{O–Zn}$) core/shell—(P_{O-N}) MB	0.310	63.441
dimer CMC- ($P_{O–Zn}$) core/shell—(P_{O-S}) MB	0.340	53.833
dimer CMC- ($P_{O–Zn}$) core/shell—(P_{OH}) MB	0.038	67.606

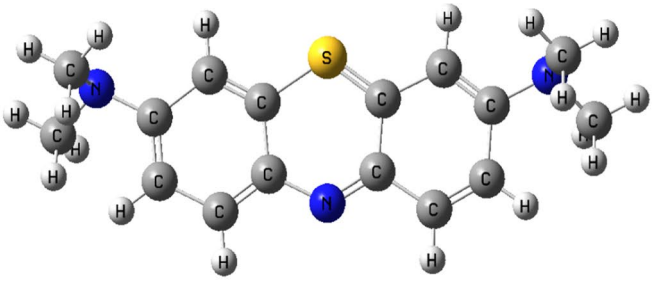

(a)

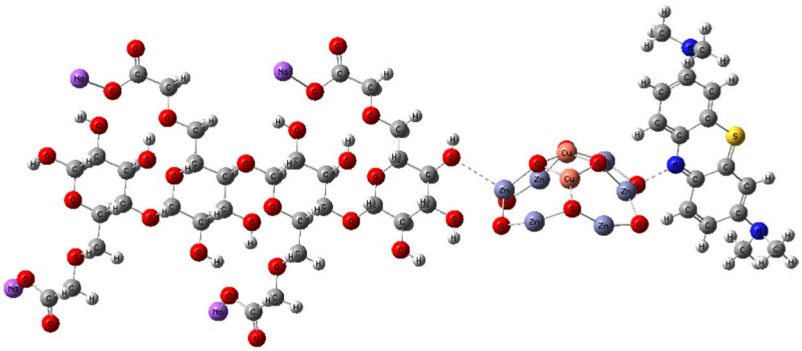

(b)

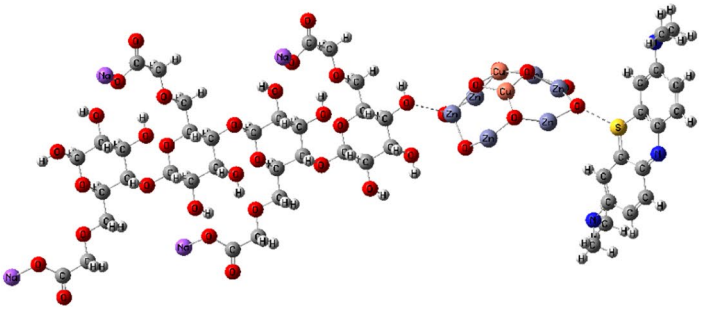

(c)

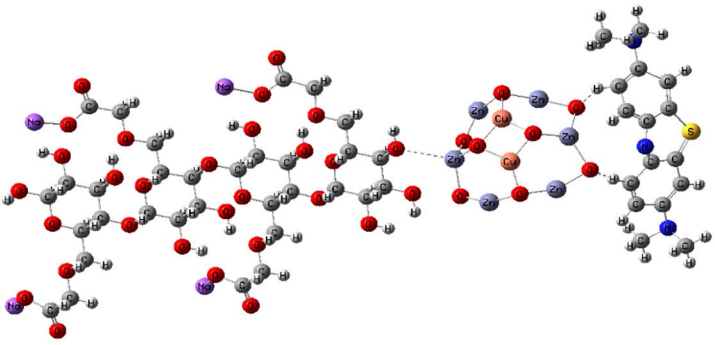

(d)

Fig. 8 MESP maps for the structure representing MB adsorption on the dimer CMC /CuO@ZnO core/shell structure's surface at different locations: **a** MB dye, **b** dimer CMC- (P_{O-Zn}) core/shell—(P_{O-N}) MB, **c** dimer CMC- (P_{O-Zn}) core/shell—(P_{O-S}) MB and **d** dimer CMC- (P_{O-Zn}) core/shell—(P_{OH}) MB as contour action

(Fig. 6) compared to that of reference (Badry et al. 2022b). This result agrees well with the TDM and HOMO/LUMO bandgap results. Thus, it can be concluded that the nanocomposite structures based on CMC/ CuO@ZnO core/shell can be utilized as a gas sensor for H_2S gas. It is obvious that the red color was focused on the O atoms of the core/shell whereas the yellow color was localized on the Zn atoms. This elucidated that the O atoms are electron-rich centers and the Zn atoms are electron-deficient centers. This means that the dimer CMC becomes more sensitive and reactive due to the interaction with the CuO@ZnO core/shell.

However, for dimer CMC/CuO@ZnO core/shell interacted with NH_3 and HBr gases, the MESP maps showed significant changes. Figure 6e and f present the MESP maps of CMC/CuO@ZnO core/shell/ NH_3 gas and CMC/ CuO@ZnO core/shell/ HBr gas as a contour action calculated at the B3LYP/Lanl2DZ level of theory. These maps show that the electronic charges are redistributed within the whole structure of dimer CMC/ CuO@ZnO core/shell which means that the whole structure becomes more reactive, not just the interaction site as in the case of H_2S gas adsorption. Additionally, the intensity of the red color increased, and the whole structure became charged. The results confirmed that the sensitivity of the dimer CMC/CuO@ZnO core/shell structure to NH_3 and HBr gases is higher than that of H_2S.

2.5 Sensitivity of CMC/CuO@ZnO core/shell to methylene blue dye

Several research studies on the removal of methylene blue dye (MB) in aqueous environments have demonstrated that due to the electrostatic interaction, this dye can be effectively trapped on the metal oxide surface (Karavasilis and Tsakiroglou 2022; Hosseini et al. 2022; Mahanta et al. 2022). As a result, the oxygen atoms of the CuO@ZnO core/shell surface most likely form negatively charged regions that are able to attract the MB molecule's positive areas, facilitating the dye adsorption.

In this section, the essential factors that are responsible for the sensitivity and reactivity of the investigated structures were examined to acquire more data on the adsorption of the MB molecule on the dimer CMC/CuO@ZnO surface. HOMO/LUMO energy and TDM are two essential properties that are widely used to define the chemical reactivity of a system (Badry et al. 2022b; Refaat et al. 2019).

Table 5 shows the HOMO/LUMO energy and TDM of the dimer CMC/CuO@ZnO structure after MB adsorption. Nonetheless, from the bandgap perspective, the HOMO/LUMO bandgap energy was regarded as a crucial chemical reactivity factor. Small bandgap energy indicates high reactivity (poor chemical stability), and large bandgap energy indicates low reactivity (high chemical stability). According to the results shown in Table 5, MB has a strong interaction with the dimer CMC/CuO@ZnO surface. This is due to the large decrease in the HOMO/LUMO energy value of MB upon the interaction with dimer CMC/CuO@ZnO. MB has a HOMO/LUMO energy of 1.822 eV and a TDM of 1.646 Debye.

For the adsorption of MB on the dimer CMC/CuO@ZnO surface, the HOMO/LUMO energy, TDM, and MESP were calculated only for the interaction that proceeds through

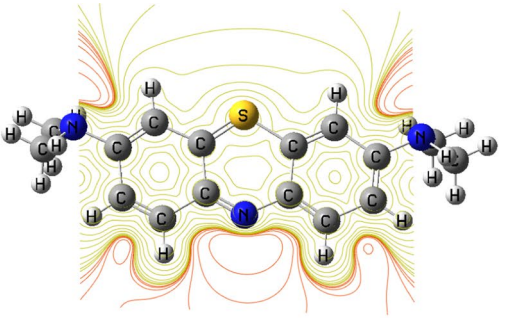

(a)

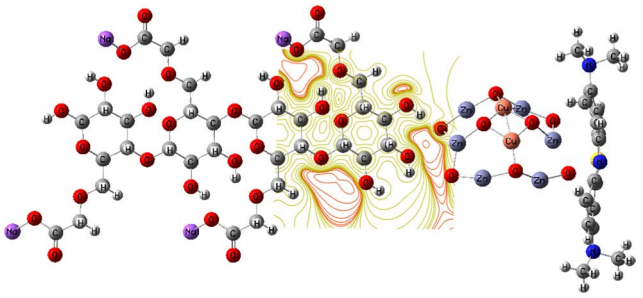

(b)

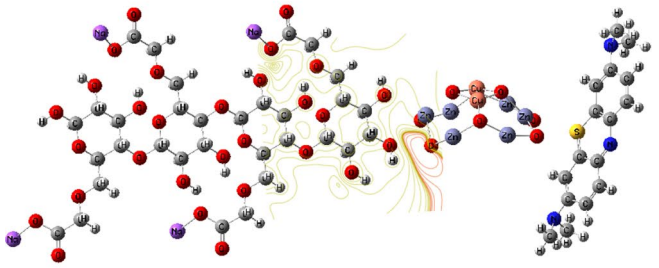

(c)

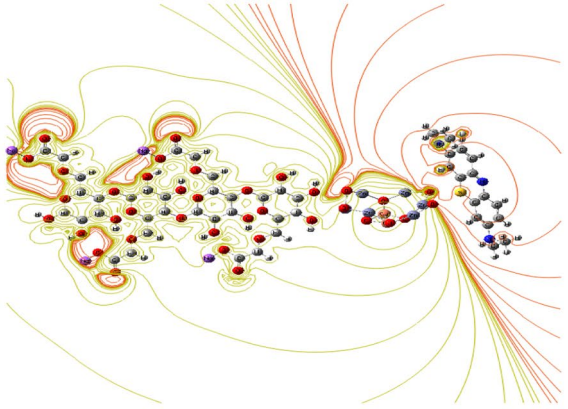

(d)

Table 6 Comparison between the HOMO/LUMO band gap energy as (eV) and TDM as Debye of CMC/CuO@ZnO core/shell and other materials reported in the literature

Structure	ΔE (eV)	TDM (Debye)	Refs.
CMC/CuO@ZnO core/shell	0.212	64.568	Present work
4 PVA-4PP	1.039	8.118	Badry et al. (2021a)
$Cu_2Zn_{10}O_{12}$	1.60	5.75	Albargi et al. (2021)
Cellulose/GO	0.360	28.524	Ezzat et al (2021)
CMC/PVP/CuO	3.185	-	Alsheheri et al (2023)

Where, the abbreviations PVA, GO, and PVP are stands for polyvinyl alcohol, graphene oxide, and polyvinylpyrrolidone, respectively

the dimer CMC's oxygen atom and the core/shell's zinc atom, i.e., the structure representing dimer CMC—($P_{O–Zn}$) core/shell. This structure has the highest interaction probability. Similarly, the sensitivity of dimer CMC/CuO@ZnO surfaces to MB was studied at different interaction sides than that stated in the last section of H_2S gas (see Fig. 7). Changing the interaction side results in changing the values of both HOMO/LUMO energy and TDM. Where, HOMO/LUMO energy changed to 0.310, 0.340, and 0.038 eV, while TDM changed to 63.441, 53.833, and 67.606 Debye. According to the findings of Tables 4 and 5, it can be concluded that the adsorption of H_2S and MB throughout the oxygen atom of the core/shell is more probable to occur than other interaction hypotheses since this has a lower bandgap energy and higher TDM values.

Figure 8 shows the MESP maps as a contour action for MB adsorbed on the dimer CMC/CuO@ZnO surface. It can be demonstrated that the S and N atoms are the negatively charged adsorbent sites. Figure 7 confirms nucleophilic and electrophilic assaults on the dimer CMC/ CuO@ZnO core/shell and MB surfaces. The appearance of a light green color as a result of the strong electrostatic interaction between the dimer CMC/CuO@ZnO and MB, which refers to a neutrally charged surface, indicates a strong interaction between them.

Table 6 presents a comparison between the HOMO/LUMO band gap energy as (eV) and TDM as Debye of the proposed structure of CMC and CMC/CuO@ZnO core/shell with other materials reported in the literature. The table confirmed that the dimer CMC/CuO@ZnO core/shell model molecule has the lowest HOMO/LUMO band gap energy and highest TDM values in comparison with the other models reported in the literature. Accordingly, the dimer CMC/CuO@ZnO structure is a promising candidate for H_2S, NH_3, HBr gases, and MB dye.

3 Conclusion

Toxic gases and dyes like H_2S, NH_3, HBr, and MB dye are harmful to human health even at very low concentrations. As a result, reliable detection of multiple low-concentration gases and dyes is required for environmental monitoring, industrial facilities, automotive, air quality assurance technologies, and many other applications. The B3LYP/Lanl2dz model has been used to conduct a theoretical investigation of the effects of the CuO@ZnO core/ shell on the sensitivity of CMC nanocomposite. TDM, HOMO/LUMO

energy, and MESPs are estimated for all models of CMC and CuO@ZnO core/shell nanocomposite. In this study, TD-DFT was used to determine the UV–Vis absorption spectra of CuO, ZnO, and CuO@ZnO core/shell structures. The obtained results for CuO and ZnO molecules are in good agreement with the experimental results. This confirms that the Lanl2dz basis set is suitable for studying the optical properties of metal oxides. The calculated TDM for dimer CMC/ CuO@ZnO structure reached 72.152, 66.644, 73.607, and 67.606 Debye upon exposure to H_2S, NH_3, HBr, and MB, respectively, which revealed the strong interaction between the investigated H_2S, NH_3, HBr, and MB and dimer CMC/ CuO@ZnO structure. The HOMO/LUMO bandgap energy of the dimer CMC/CuO@ZnO structure was reduced due to this interaction by 6.42% and 82.57% for H_2S and MB dye, respectively. Because of this, the dimer CMC/CuO@ZnO structure was more vulnerable to MB dye than to H_2S gas. Additionally, MESP maps revealed that the reactivity of dimer CMC improved strongly due to the interaction with the CuO@ZnO core/shell. The red and yellow regions extended to the H_2S, NH_3, HBr, and MB locations, which confirmed the increased electronegativity of the dimer CMC/CuO@ZnO structure upon the adsorption of H_2S, NH_3, HBr, and MB on its surface. According to our current findings about the changes that have occurred in the electronic properties of the dimer CMC/CuO@ZnO structure due to the adsorption of H_2S, NH_3, HBr, and MB, the dimer CMC/CuO@ZnO structure may be a promising nanomaterial for the detection of H_2S, NH_3, HBr gases, and MB dye.

Authors' contributions RB conduct experimental part, writing the paper. NN supervising the work and assign the problem. MMEN Assign the problem, supervise the work. HE writing the paper. MAI, conducting calculations and co-writing the paper.

Funding Open access funding provided by The Science, Technology & Innovation Funding Authority (STDF) in cooperation with The Egyptian Knowledge Bank (EKB). There is no funding received.

Data availability The data will be available upon request.

Declarations

Competing interests I declare that the authors have no competing interests as defined by Springer, or other interests that might be perceived to influence the results and/or discussion reported in this paper.

Ethical approval This work is not applicable for both human and/ or animal studies.

References

Abd-Elhamid, A.I., Emran, M., El-Sadek, M.H., El-Shanshory, A.A., Soliman, H.M.A., Akl, M.A., Rashad, M.: Enhanced removal of cationic dye by eco-friendly activated biochar derived from rice straw. Appl Water Sci **10**, 45 (2020). https://doi.org/10.1007/s13201-019-1128-0

Albargi, H., Ammar, H.Y., Badran, H.M., Algadi, H., Umar, A.: P-CuO/n-ZnO heterojunction structure for the selective detection of hydrogen sulphide and sulphur dioxide gases: a theoretical approach. Coatings **11**(10), 1200 (2021). https://doi.org/10.3390/coatings11101200

Alsheheri, S., Alamshany, Z., Abdelaal, M.Y.: Preparation and physicochemical studies on polymeric nanocomposites containing copper oxide nanoparticles. Des. Monomers Polym. **26**(1), 68–76 (2023). https://doi.org/10.1080/15685551.2023.2190222

Amu-Darko, J.N.O., et al.: Metal-organic frameworks-derived In_2O_3/ZnO porous hollow nanocages for highly sensitive H_2S gas sensor. Chemosphere **314**, 137670 (2023). https://doi.org/10.1016/j.chemosphere.2022.137670

Badry, R., Fahmy, A., Ibrahim, A., Elhaes, H., Ibrahim, M.: Application of polyvinyl alcohol/polypropylene/zinc oxide nanocomposites as sensor: modeling approach. Opt. Quantum Electron. **53**(1), 1–12 (2021b). https://doi.org/10.1007/s11082-020-02646-5

Badry, R., Hegazy, M., Yahia, I., Elhaes, H., Zahran, H., Abdel-Salam, A., Matar, H., Ibrahim, M.: Enhancing the optical properties of starch/ZnO nanocomposites using graphene oxide. Egypt. J. Chem. **65**(7), 335–342 (2022a). https://doi.org/10.21608/EJCHEM.2021.104153.4811

Badry, R., Nada, N., El-Nahass, M.M., Elhaes, H., Ibrahim, M.A.: The detection of NH_3, H_2S and HBr gases by carboxymethyl cellulose sodium/ZnO nanocomposites: a theoretical study. Egypt. J. Chem. **65**(7), 281–292 (2022b). https://doi.org/10.21608/EJCHEM.2021.103668.4797

Becke, A.D.: A new mixing of Hartree-Fock and local density-functional theories. J. Chem. Phys. **98**(2), 1372–1377 (1993a). https://doi.org/10.1063/1.464304

Becke, A.D.: Density-functional thermochemistry. III. The role of exact exchange. J. Chem. Phys. **98**, 5648–5652 (1993b). https://doi.org/10.1063/1.464913

Chahar, D., Kumar, D., Thakur, P., Thakur, A.: Visible light induced photocatalytic degradation of methylene blue dye by using Mg doped Co–Zn nanoferrites. Mater. Res. Bull. **162**, 112205 (2023). https://doi.org/10.1016/j.materresbull.2023.112205

Chauhan, R., Kaur, H., Alankar, B.: Air quality forecast using convolutional neural network for sustainable development in urban environments. Sustain. Cities Soc. **75**, 103239 (2021). https://doi.org/10.1016/j.scs.2021.103239

Chen, H., Ao, S., Li, G.D., Gao, Q., Zou, X., Wei, C.: Enhanced sensing performance to toluene and xylene by constructing $NiGa_2O_4$–NiO heterostructures. Sens. Actuators B Chem. **282**, 331–338 (2019). https://doi.org/10.1016/j.snb.2018.11.072

Cui, L., Zhou, J., Peng, X., Ruan, S., Zhang, Y.: Analyses of air pollution control measures and co-benefits in the heavily air-polluted Jinan city of China, 2013–2017. Sci. Rep. **10**(1), 1–10 (2020). https://doi.org/10.1038/s41598-020-62475-0

Dadkhah, M., Tulliani, J.M.: Green synthesis of metal oxides semiconductors for gas sensing applications. Sensors **22**(13), 4669 (2022). https://doi.org/10.3390/s22134669

Dey, S., Nag, S., Santra, S., Ray, S.K., Guha, P.K.: Voltage-controlled NiO/ZnO p–n heterojunction diode: a new approach towards selective VOC sensing. Microsyst. Nanoeng. **6**(1), 1–9 (2020). https://doi.org/10.1038/s41378-020-0139-1

Eltaweil, A.S., Abd El-Monaem, E.M., El-Subruiti, G.M., Ali, B.M., Abd El-Latif, M.M., Omer, A.M.: Graphene oxide incorporated cellulose acetate beads for efficient removal of methylene blue dye; isotherms, kinetic, mechanism and co-existing ions studies. J. Porous Mater. **30**(2), 607–618 (2023). https://doi.org/10.1007/s10934-022-01347-6

Ezzat, H.A., Hegazy, M.A., Nada, N.A., Osman, O., Ibrahim, M.A.: Development of natural polymer/metal oxide nanocomposite reinforced with graphene oxide for optoelectronic applications. NRIAG J. Astron. Geophys. **10**(1), 10–22 (2021). https://doi.org/10.1080/20909977.2020.1846246

Feng, X., Zhang, Y., Wang, Z.: Theoretical study of piezotronic heterojunction. Sci. China Technol. Sci. **56**, 2615–2621 (2013). https://doi.org/10.1007/s11431-013-5358-3

Foresman, J., Frish, E.: Exploring chemistry. Gaussian Inc., Pittsburg (1996). https://doi.org/10.4236/ojinm.2015.52004

Frisch, M.J., Trucks, G.W., Schlegel, H.B. , Scuseri, G.E., Robb, M.A., Cheeseman, J.R., Scalmani, G., Barone, V., Mennucci, P.B.G.A., Nakatsuji, H., Caricato, M., Li, X., Hratchian, P.HI., Izmaylov, A.F., Bloino, J., Zheng, G., Sonnenberg, J.L., Hada, M., Ehara, M., Toyota, K., Fukuda, R., Hasegawa, J., Ishida, M., Nakajima, T., Honda, Y., Kitao, O., Nakai, H., Vreven, T., Montgomery, J.A., Jr.,. Peralta, J.E., Ogliaro, F.;,Bearpark, M., Heyd, J.J., Brother, E., Kudin, K.N., Staroverov,

V.N., Keith, T., Kobayashi, R., Normand, J., Raghavachari, K., Rendell, A., Burant, J.C., Iyengar, S.S., Tomasi, J., Cossi, M., Rega, N., Millam, J.M., Klene, M., Knox, J.E., Cross, J.B., Bakken, V., Adamo, C., Jaramillo, J., Gomperts, R., Stratmann, R.E., Yazyev, O., Austin, A.J., Cammi, R., Pomelli, C., Ochterski, J.W., Martin, R.L., Morokuma, K., Zakrzewski, V.G., Voth, G.A., Salvador, P., Dannenberg, J.J., Dapprich, S., Daniels, A.D., Farkas, O., Foresman, J.B., Ortiz, J.V., Cioslowski, J., Fox, D.J.: Gaussian 09, Revision C.01 , Gaussian, Inc.; Wallingford CT (2010)

Gai, L.Y., Lai, R.P., Dong, X.H., Wu, X., Luan, Q.T., Wang, J., et al.: Recent advances in ethanol gas sensors based on metal oxide semiconductor heterojunctions. Rare Met. **41**(6), 1818–1842 (2022). https://doi.org/10.1007/s12598-021-01937-4

Hosseini, H., Zirakjou, A., McClements, D.J., Goodarzi, V., Chen, W.H.: Removal of methylene blue from wastewater using ternary nanocomposite aerogel systems: Carboxymethyl cellulose grafted by polyacrylic acid and decorated with graphene oxide. J. Hazard. Mater. **421**, 126752 (2022). https://doi.org/10.1016/j.jhazmat.2021.126752

Hosseini-Shokouh, S.H., Zhou, J., Berger, E., Lv, Z.P., Hong, X., Virtanen, V., et al.: Highly selective H_2S gas sensor based on Ti3C2Tx MXene–organic composites. ACS Appl. Mater. Interfaces **15**(5), 7063–7073 (2023). https://doi.org/10.1021/acsami.2c19883

Isaac, N.A., Pikaar, I., Biskos, G.: Metal oxide semiconducting nanomaterials for air quality gas sensors: operating principles, performance, and synthesis techniques. Microchim. Acta **189**(5), 1–22 (2022). https://doi.org/10.1007/s00604-022-05254-0

Jung, K., Lim, T., Li, Y., Martinez-Morales, A.A.: ZnO–CuO core–shell heterostructure for improving the efficiency of ZnO-based dye-sensitized solar cells. MRS Adv. **2**(15), 857–862 (2017). https://doi.org/10.1557/adv.2017.247

Karaduman Er, I., Sarf, F., Yakar, E.: Investigation of H_2S gas sensing performance of Ni: WO_3 films at room temperature: nickel precursor effect. J. Mater. Sci. Mater. Electron. **33**(6), 3397–3410 (2022). https://doi.org/10.1007/s10854-021-07537-3

Karavasilis, M.V., Tsakiroglou, C.D.: Use of immobilized zinc oxide photocatalysts for wastewater treatment: application to methylene blue degradation. Canad. J Chem. Eng. **100**(5), 893–910 (2022). https://doi.org/10.1002/cjce.24199

Khan, I., Khan, I., Usman, M., Imran, M., Saeed, K.: Nanoclay-mediated photocatalytic activity enhancement of copper oxide nanoparticles for enhanced methyl orange photodegradation. J. Mater. Sci. Mater. Electron. **31**, 8971–8985 (2020). https://doi.org/10.1007/s10854-020-03431-6

Kumar, R.R., et al.: Ultrasensitive and light-activated NO2 gas sensor based on networked MoS_2/ZnO nanohybrid with adsorption/desorption kinetics study. Appl. Surface Sci. **536**, 147933 (2021). https://doi.org/10.1016/j.apsusc.2020.147933

Lee, C., Yang, W.T., Parr, R.G.: Development of the Colle-Salvetti correlation-energy formula into a functional of the electron density. Phys. Rev. B **37003A**, 785–789 (1988). https://doi.org/10.1103/PhysRevB.37.785

Li, T.T., Bao, N., Geng, A.F., Yu, H., Yang, Y., Dong, X.T.: Study on room temperature gas-sensing performance of CuO film-decorated ordered porous ZnO composite by In_2O_3 sensitization. R. Soc. Open Sci. **5**(2), 171788 (2018). https://doi.org/10.1098/rsos.171788

Li, X., et al.: Exposed edges of porous ultrathin WO_3 nanosheets determined High-performance sensing for hydrogen sulfide. Appl. Surface Sci. **571**, 151327 (2022a). https://doi.org/10.1016/j.apsusc.2021.151327

Li, Z., et al.: Metal-organic framework-derived ZnO decorated with CuO for ultra-high response and selectivity H_2S gas sensor. Sens. Actuators B Chem. **366**, 131995 (2022b). https://doi.org/10.1016/j.snb.2022.131995

Li, Z., Lai, Z., Zhao, Z., Zhang, L., Jiao, W.: A high-performance gas sensor for the detection of H_2S based on Nd_2O_3-doped ZnO nanoparticles. Sens. Actuators A **350**, 114119 (2023). https://doi.org/10.1016/j.sna.2022.114119

Mahanta, U., Khandelwal, M., Deshpande, A.S.: TiO_2@SiO_2 nanoparticles for methylene blue removal and photocatalytic degradation under natural sunlight and low-power UV light. Appl. Surf. Sci. **576**, 151745 (2022). https://doi.org/10.1016/j.apsusc.2021.151745

Manisalidis, I., Stavropoulou, E., Stavropoulos, A., Bezirtzoglou, E.: Environmental and health impacts of air pollution: a review. Front. Public Health **8**, 14 (2020). https://doi.org/10.3389/fpubh.2020.00014

Navale, Y.H., Navale, S.T., Chougule, M.A., Ramgir, N.S., Patil, V.B.: NO_2 gas sensing properties of heterostructural CuO nanoparticles/ZnO nanorods. J. Mater. Sci. Mater. Electron. **32**(13), 18178–18191 (2021). https://doi.org/10.1016/j.ceramint.2018.10.022

Nemufulwi, M.I., Swart, H.C., Shingange, K., Mhlongo, G.H.: ZnO/$ZnFe_2O_4$ heterostructure for conductometric acetone gas sensors. Sens. Actuators B Chem. **377**, 133027 (2023). https://doi.org/10.1016/j.snb.2022.133027

Obayomi, K.S., et al.: Green synthesis of graphene-oxide based nanocomposites for efficient removal of methylene blue dye from wastewater. Desalination (2023). https://doi.org/10.1016/j.desal.2023.116749

Omar, A., et al.: Enhancing the optical properties of chitosan, carboxymethyl cellulose, sodium alginate modified with nano metal oxide and graphene oxide. Opt. Quantum Electron. **54**(12), 806 (2022). https://doi.org/10.1007/s11082-022-04107-7

Politzer, P., Laurence, P.R., Jayasuriya, K.: Molecular electrostatic potentials: an effective tool for the elucidation of biochemical phenomena. Environ. Health Perspect. **61**, 191–202 (1985). https://doi.org/10.1289/ehp.8561191

Pullman, A., Pullman, B.: Molecular electrostatic potential of the nucleic acids. Q. Rev. Biophys. **14**(3), 289–380 (1981). https://doi.org/10.1017/S0033583500002341

Rani, S., et al.: Temperature-dependent n–p–n switching and highly selective room-temperature n-$SnSe_2$/p-SnO/n-SnSe heterojunction-based NO_2 gas sensor. ACS Appl. Mater. Interfaces **14**(13), 15381–15390 (2022). https://doi.org/10.1021/acsami.1c24679

Refaat, A., et al.: Geometrical, vibrational and physical properties of polyvinyl chloride nanocomposites: molecular modeling approach. J. Theor. Comput. Chem. **18**(08), 1950037 (2019). https://doi.org/10.1142/S0219633619500378

Rui-Jie, W.U., Xue-Min, T.I.A.N., Zhong-Qiu, H.U.A., Ning, L.U., Pan, W.A.N.G.: A low temperature catalytic combustible gas sensor based on Ru supported zeolite catalyst films. Chin. J. Anal. Chem. **49**(11), 63–68 (2021). https://doi.org/10.1016/j.cjac.2021.07.007

Sharma, B., Sharma, A., Joshi, M., Myung, J.H.: Sputtered SnO_2/ZnO heterostructures for improved NO_2 gas sensing properties. Chemosensors **8**(3), 67 (2020). https://doi.org/10.3390/chemosensors8030067

Sun, L., Yuan, X., Sun, J., Zhang, K., Liao, D., Chen, S.: Bimetallic organic framework-derived SnO_2/Co_3O_4 heterojunctions for highly sensitive acetone sensors. New J. Chem. **45**(38), 18150–18157 (2021). https://doi.org/10.1039/D1NJ03025F

Sun, K., Zhan, G., Zhang, L., Wang, Z., Lin, S.: Highly sensitive NO2 gas sensor based on ZnO nanoarray modulated by oxygen vacancy with Ce doping. Sens. Actuators B Chem. **379**, 133294 (2023). https://doi.org/10.1016/j.snb.2023.133294

Tamura, S., Imanaka, N.: Solid electrolyte-type gas sensors applied trivalent cation conducting solid electrolytes. Sens. Actuators B Chem. **368**, 132252 (2022). https://doi.org/10.1016/j.snb.2022.132252

Vosko, S.H., Wilk, L., Nusair, M.: Accurate spin-dependent electron liquid correlation energies for local spin density calculations: a critical analysis. Can. J. Phys. **58**(8), 1200–1211 (1980). https://doi.org/10.1139/p80-159

Wan, H., Liu, X., Wang, X., Chen, Y., Wang, P.: Facile screen-printed carbon nanotube electrode on porous substrate with gold nanoparticle modification for rapid electrochemical gas sensing. J. Electrochem. Soc. **168**(6), 067514 (2021). https://doi.org/10.1149/1945-7111/ac064e

Wang, C.N., Li, Y.L., Gong, F.L., Zhang, Y.H., Fang, S.M., Zhang, H.L.: Advances in doped ZnO nanostructures for gas sensor. Chem. Rec. **20**(12), 1553–1567 (2020a). https://doi.org/10.1002/tcr.202000088

Wang, X., Li, S., Xie, L., Li, X., Lin, D., Zhu, Z.: Low-temperature and highly sensitivity H_2S gas sensor based on ZnO/CuO composite derived from bimetal metal-organic frameworks. Ceram. Int. **46**(10), 15858–15866 (2020b). https://doi.org/10.1016/j.ceramint.2020.03.133

Wang, J., Yang, Y., Xia, Y.: Mesoporous MXene/ZnO nanorod hybrids of high surface area for UV-activated NO_2 gas sensing in ppb-level. Sens. Actuators B Chem. **353**, 131087 (2022a). https://doi.org/10.1016/j.snb.2021.131087

Wang, L., Ma, X., Huang, G., Lian, R., Huang, J., She, H., Wang, Q.: Construction of ternary CuO/$CuFe_2O_4$/g-C_3N_4 composite and its enhanced photocatalytic degradation of tetracycline hydrochloride with persulfate under simulated sunlight. J. Environ. Sci. **112**, 59–70 (2022b). https://doi.org/10.1016/j.jes.2021.04.026

Wang, Y., et al.: CuO/WO_3 hollow microsphere PN heterojunction sensor for continuous cycle detection of H2S gas. Sens. Actuators B Chem. **374**, 132823 (2023). https://doi.org/10.1016/j.snb.2022.132823

Weiner, P.K., Langridge, R., Blaney, J.M., Schaefer, R., Kollman, P.A.: Electrostatic potential molecular surfaces. Proc. Natl. Acad. Sci. u.s.a. **79**(12), 3754–3758 (1982). https://doi.org/10.1073/pnas.79.12.3754

Wu, Z., et al.: An all-inorganic type-II heterojunction array with nearly full solar spectral response based on ZnO/ZnSe core/shell nanowires. J. Mater. Chem.y **21**(16), 6020–6026 (2011). https://doi.org/10.1039/C0JM03971C

Wu, R., et al.: A selective methane gas sensor based on metal oxide semiconductor equipped with an on-chip microfilter. Sens. Actuators B Chem. **359**, 131557 (2022). https://doi.org/10.1016/j.snb.2022.131557

Yin, X.T., et al.: Opposite sensing response of heterojunction gas sensors based on SnO_2–Cr_2O_3 nanocomposites to H2 against CO and its selectivity mechanism. Langmuir **37**(46), 13548–13558 (2021). https://doi.org/10.1021/acs.langmuir.1c01706

Zhang, J., Ma, S., Wang, B., Pei, S.: Preparation of composite SnO_2/CuO nanotubes by electrospinning and excellent gas selectivity to ethanol. Sens. Actuators A **332**, 113090 (2021). https://doi.org/10.1016/j.sna.2021.113090